



# Readily achieving concentration-tunable oxygen vacancies in $\text{Bi}_2\text{O}_2\text{CO}_3$ : Triple-functional role for efficient visible-light photocatalytic redox performance

Shixin Yu<sup>a</sup>, Yihe Zhang<sup>a,\*</sup>, Fan Dong<sup>b</sup>, Min Li<sup>a</sup>, Tierui Zhang<sup>c</sup>, Hongwei Huang<sup>a,\*</sup>

<sup>a</sup> Beijing Key Laboratory of Materials Utilization of Nonmetallic Minerals and Solid Wastes, School of Materials Science and Technology, China University of Geosciences, Beijing 100083, China

<sup>b</sup> College of Environmental and Biological Engineering, Chongqing Technology and Business University, Chongqing 400067, China

<sup>c</sup> Key Laboratory of Photochemical Conversion and Optoelectronic Materials, Technical Institute of Physics and Chemistry, Chinese Academy of Sciences, Beijing 100190, China

## ARTICLE INFO

### Keywords:

Photocatalysis

$\text{Bi}_2\text{O}_2\text{CO}_3$

Concentration-tunable oxygen vacancy

Band structure

$\text{H}_2$  evolution

## ABSTRACT

Crystal defects of semiconductor materials exert huge impact on their physical and chemical properties. Herein, we report the development of oxygen vacancy (OV) concentration-tunable  $\text{Bi}_2\text{O}_2\text{CO}_3$  (BOC) via a facile and scalable precipitation approach with assistance of glyoxal as reductant at atmospheric environment. Introduction of OV takes a triple-functional role in regulating the band structure and charge movement behaviors of BOC. It not only renders appearance of defect band level in the forbidden band, allowing BOC drastically extended photoabsorption from 360 to 520 nm, but also tremendously promotes the charge carrier density, bulk charge separation, surface charge separation and interfacial charge transfer. In contrast to pristine BOC, OV-BOC demonstrates highly promoted photocatalytic performance for water splitting into  $\text{H}_2$  evolution, NO removal from the gas phase and degradation of a typical antibiotic tetracycline hydrochloride, where the  $\text{H}_2$  production is first reported for BOC. Additionally, the OV concentration of BOC can be continuously modulated only by regulating the concentration of glyoxal, thereby achieving the adjustable photoabsorption and band structure. Our work enables smart design on oxygen vacancy-activated photocatalytic materials for solar-energy-conversion applications through a readily achievable tactic.

## 1. Introduction

Semiconductor photocatalysis is deemed to be a promising strategy to solve the environmental and energy issues by utilizing solar energy [1–3]. Crystal and surface structures of semiconductor materials significantly influence their physical and chemical properties [4,5]. Vacancies play a crucial role in ameliorating the performance of photocatalysts by introduction of adventitious energy levels and serving as reactive sites [6]. Particularly, fabrication of surface disordered anatase  $\text{TiO}_2$  nanocrystals via hydrogenation opened the window for engineering oxide photocatalysts through manufacturing abundant oxygen vacancies (OV) [7]. As a typical crystal defect, OV can narrow the band gap of semiconductors by forming OV state between conduction band (CB) and valence band (VB) to expend the photo-responsive range [8–10]. So far, generation of OV in photocatalysts is mainly achieved by heating treatment under vacuum [11], hydrogen atmosphere [12,13], or solvothermal process [14], which are subject to

harsh reaction atmosphere (e.g. high temperature and pressure), complex synthesis procedure, etc. [15]. Meanwhile, control on the OV concentration that may adjust the band energy level of semiconductors and optimize the photocatalytic activity has been seldom achieved yet. Therefore, facily creating OV at ambient atmosphere with adjustable vacancy concentrations is highly challenging and appealing.

Recently, Bi-based semiconductor photocatalysts, especially Aurivillius structured  $\text{Bi}_2\text{XO}_6$  ( $\text{X} = \text{W}, \text{Mo}$ ) [16,17], Sillén structured  $\text{BiOX}$  ( $\text{X} = \text{Cl}, \text{Br}, \text{I}$ ) [14,18], etc, have triggered the interests of scientists because of their unordinary layered crystal structure, which can induce strong internal static electric field and consequently promote the separation and transfer of photoinduced charges [19,20].  $\text{Bi}_2\text{O}_2\text{CO}_3$  (BOC) is an unique Bi-based semiconductor with Aurivillius/Sillén-related structured layered structure, which is composed of alternating  $[\text{Bi}_2\text{O}_2]^{2+}$  slices and  $\text{CO}_3^{2-}$  anions [21]. It has been intensively studied as a UV-light responsive photocatalyst for removal of gaseous pollutants (e.g. NO) and liquid contaminants [22,23]. Yet, BOC has a wide band

\* Corresponding authors.

E-mail addresses: [zyh@cugb.edu.cn](mailto:zyh@cugb.edu.cn) (Y. Zhang), [hwh@cugb.edu.cn](mailto:hwh@cugb.edu.cn) (H. Huang).

gap of 3.3–3.5 eV, in which the insufficient light absorption of severely restrict its application in visible-light region, which constitutes the most of solar spectrum [24–28]. In consideration of the high oxygen content (62.5% of O atomic percentage) and structural/optical features of BOC, it may be a proper model to explore the effects of OV on band structure modulation and visible-light photocatalytic performance.

In this work, we report the synthesis of BOC with oxygen vacancies (OV-BOC) via a facile precipitation route at room temperature by utilizing glyoxal as the reductant. Herein, glyoxal has a moderate reduction ability [29], which is proved to be critical for yielding oxygen vacancies and resulting in the target material. Compared to BOC, the photoabsorption in OV-BOC is drastically extended to visible light region. The photocatalytic activity of samples is systematically investigated by hydrogen production from water, NO removal and degradation of antibiotic. The surface structure, band structure and charge movement are detailedly analyzed to elucidate the as-achieved much improved photocatalytic performance. Besides, the continuously-adjustable OV concentration of BOC is demonstrated by simply controlling the addition content of glyoxal, which renders adjustable photoabsorption in visible light region.

## 2. Experimental section

### 2.1. Synthesis

The chemicals used in this work are of analytical grade and without further treatment. The pristine BOC sample was prepared by a simple solution precipitation method at room temperature. 2 mmol Bi(NO<sub>3</sub>)<sub>3</sub>·5H<sub>2</sub>O (Xilong Scientific Co., Ltd.) and 8 mmol Na<sub>2</sub>CO<sub>3</sub> (Beijing Chemical Industry Group CO., Ltd) were dispersed in 20 mL ethylene glycol (EG) (Beijing Chemical Industry Group CO., Ltd) and 20 mL deionized water, respectively, with a short time supersonic treatment and magnetic stirring. The Na<sub>2</sub>CO<sub>3</sub> solution was added drop wise into the Bi(NO<sub>3</sub>)<sub>3</sub>·5H<sub>2</sub>O solution under magnetic stirring. After 12 h reaction, the power product was collected and washed with alcohol and deionized water for 4 times and dried at 60 °C. With respect to synthesis of OV-BOC, 2 mmol Bi(NO<sub>3</sub>)<sub>3</sub>·5H<sub>2</sub>O was dispersed in 20 mL EG and 2 mL glyoxal (40% aqueous solution) (Xilong Scientific Co., Ltd.), and 8 mmol Na<sub>2</sub>CO<sub>3</sub> was dispersed in 20 mL deionized water. Then, the following procedures are same with that of BOC, and OV-BOC samples with different OV concentrations are denoted as OV-BOC #1, OV-BOC #2 and OV-BOC #3 with the added glyoxal amount of 2 mL, 3 mL and 4 mL, respectively.

### 2.2. Characterization

The phase structure of the series samples was recorded by X-ray diffraction (XRD) in a Bruker D8 Advance diffractometer with Cu K $\alpha$  radiation. The Fourier-transform infrared (FTIR) spectra were measured by a Bruker spectrometer in the frequency range from 400 to 2000 cm<sup>-1</sup>. The microstructure and morphology of the photocatalysts were researched by a scanning electron microscopy (SEM, S-4800 Hitachi, Japan). Transmission electron microscopy (TEM) and high-resolution transmission electron microscopy (HRTEM) were performed on a electron microscopy (JEM-2010, JEOL, Japan). Fast Fourier transition (FFT) of HRTEM was carried out by software Gatan DigitalMicrograph. The composition and surface properties of the as-synthesized samples were investigated by X-ray photoelectron spectroscopy (XPS, ESCALAB 250 Xi ThermoFisher, USA). The optical properties were measured by UV–vis diffuse reflectance spectra (DRS) using a UV–vis spectrophotometer (Varian Cary 5000, USA). Electron paramagnetic resonance (EPR) measurement was taken on an Endor spectrometer (ES-3X, JEOL, Japan).

### 2.3. Photocatalytic H<sub>2</sub> evolution

Photocatalytic H<sub>2</sub> production experiments were performed in a sealed glass cylinder reactor with a quartz glass lid and a rubber sampling port at room temperature. A 300 W Xe lamp was used as the simulated solar light source. Before the photoreaction, 1 wt% Pt was loaded on the photocatalyst powder (50 mg) by a UV light reduction method in a mixed solution of 40 mL deionized water, 10 mL methyl alcohol (MeOH) and a certain amount of H<sub>2</sub>PtCl<sub>6</sub> for 30 min. Then, the suspension was moved into the sealed glass cylinder reactor and added 50 mL deionized water. Before turning the Xe lamp on, the air in the reactor was removed by Ar stream. After the Xe lamp on, the gas was extracted for each hour and analyzed by gas chromatography (GC7900, Techcomp limited, China) with a thermal conductivity detector.

### 2.4. Photocatalytic removal of NO

Photocatalytic removal of ppb level NO gas is conducted in a 4.5 L (30 cm × 15 cm × 10 cm) organic glass reactor with continuous NO flow. The light source is a 150 W commercial Xe lamp which is vertically placed toward the reactor and coupled with a 420 nm cutoff filter to exclude the UV light in the light beam. 0.2 g of the photocatalyst was dispersed in deionized water by ultrasonic for 10 min and coated on glass dishes with the diameter of 12 cm. The dishes were dried in 70 °C to remove all the deionized water. The 600 ppb NO gas in the measurement was acquired by diluted the 100 ppm compressed gas cylinder via flowing air. Before the photocatalytic reaction, an adsorption-desorption equilibrium was achieved in darkness. After equilibrium, the lamp was turned on. At every minute, the concentration of NO<sub>x</sub> (NO<sub>x</sub> includes NO and NO<sub>2</sub>) was measured by a NO<sub>x</sub> analyzer (Thermo Scientific, 42i-TL). The removal ratio ( $\eta$ ) of NO was calculated as  $\eta$  (%) =  $(1 - C/C_0) \times 100\%$ , where  $C$  and  $C_0$  are concentrations of NO<sub>x</sub> in the outlet stream and the inlet stream.

### 2.5. Photodegradation of tetracycline hydrochloride

Photocatalytic degradation of tetracycline hydrochloride (TC) is carried out under the irradiation of a 500 W Xe lamp with 420 nm cutoff filters. The photocatalyst powder (50 mg) was ultrasonically dispersed in 50 mL of TC solution (10 mg/L) in quartz tubes. Before starting the photocatalytic degradation, the mixtures in quartz tubes were stirred for 30 min in darkness in order to achieve an absorption-desorption equilibrium between the powders and solution. After illumination, 2.5 mL of the suspensions were extracted each hour, and separated by centrifugation to obtain the supernatant solutions. The concentrations of as-obtained solutions were measured by testing the absorbance at the characteristic bands of the TC solution. The UV–vis spectra of the supernatant solutions were recorded on a U-3010 spectrophotometer.

### 2.6. Active species trapping experiment

Active species generated in the photocatalytic reaction, involving superoxide radicals ( $\cdot\text{O}_2^-$ ), hydroxyl radicals ( $\cdot\text{OH}$ ) and holes ( $\text{h}^+$ ), were consumed by the addition of nitrogen and 1 mM isopropanol (IPA) and 1 mM potassium iodide (KI) as scavengers in TC photodegradation experiment, respectively.

### 2.7. Photoelectrochemical and photoelectric measurements

The photoelectrochemical properties, including the photocurrent response, electrochemical impedance spectrum (EIS), voltammograms (I–V) and Mott-Schottky curves, were measured in a standard three-electrode system with using an electrochemical workstation (CHI660E, Chenhua Instruments Co. Shanghai, China). In this three-electrode system, a saturated calomel electrode (SCE) was utilized as the reference electrode, and platinum wire was the counter electrode, and the

electrolyte solution was 0.1 mol/L  $\text{Na}_2\text{SO}_4$  solution. The working electrode was samples film coated on indium-tin oxide (ITO) sheet glass. And all the measurements were conducted at room temperature. Visible light photocurrent response used a 300 W Xe lamp with a 420 nm cutoff filter as the light source. Different wave length visible light photocurrent response and continuous wavelength photocurrent response used the 300 W Xe lamp with 5 bandpass filters and monochromator as the light sources, respectively. There was no voltage applied between the electrodes in photocurrent response measurements. The Mott-Schottky curves were gauged at a frequency of 100 Hz. Surface photovoltage (SPV) measurement system included a source of monochromatic light which provided by a 300 W Xe lamp and a double-prism monochromator (Zolix SBP500), a lock-in amplifier (SR830-DSP) with a light chopper (SR540) and a photovoltaic cell. Photocatalyst powder was placed between ITO electrode and a copper electrode.

### 3. Results and discussion

#### 3.1. Crystal structure, surface structure, optical absorption and oxygen vacancy

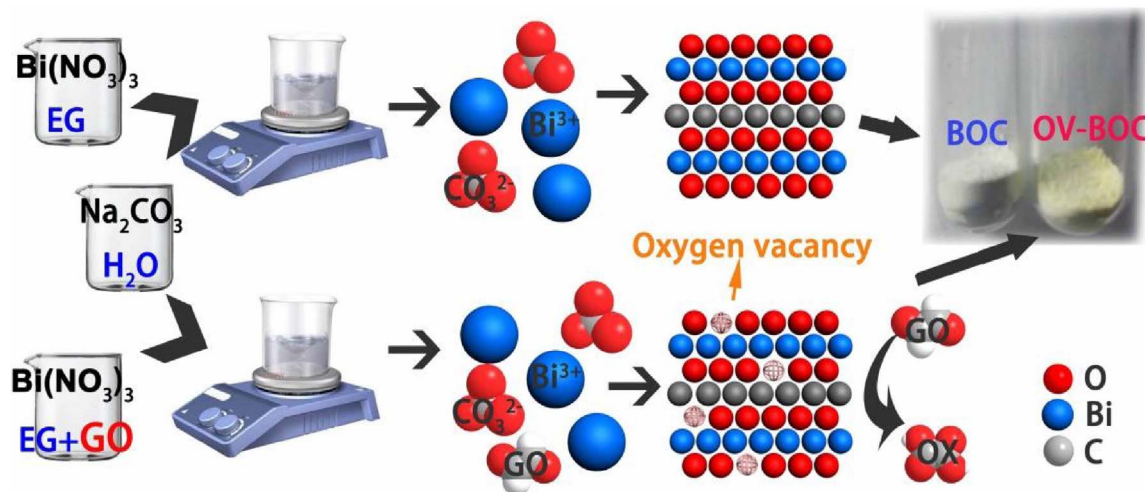
Scheme 1 displays the schematic diagram for preparation process of  $\text{Bi}_2\text{O}_2\text{CO}_3$  (BOC) and oxygen vacancy-BOC (OV-BOC). Compared with the solution composition for BOC preparation, a modicum of glyoxal was added for synthesis of OV-BOC. Because of the reducibility of glyoxal,  $\text{Bi}^{3+}$  could be reduced by glyoxal, resulting in the escaping of some oxygen atoms in BOC, and glyoxal may be oxidized into oxalic acid. BOC and OV-BOC samples were characterized by XRD and the patterns are in Fig. 1A. The two XRD patterns of BOC and OV-BOC show not any difference even a slight deviation, signifying that the preferential orientation and crystalline phase of BOC are not changed. The FTIR spectra of BOC and OV-BOC (Fig. 1B) fit well with the characteristic peaks of  $\text{Bi}_2\text{O}_2\text{CO}_3$ . The peaks at  $1467$  and  $1395\text{ cm}^{-1}$  are assigned to the anti-symmetric vibration mode  $\nu_3$  of  $\text{CO}_3^{2-}$  and the peak at  $846\text{ cm}^{-1}$  is caused by out-of-plane bending mode  $\nu_2$   $\text{CO}_3^{2-}$ . The Bi–O vibration peak is located at  $546\text{ cm}^{-1}$  [30]. These observations proved that OV-BOC possesses the same functional groups with pure BOC. Based on the results from XRD and FTIR, it can be concluded that the crystal structure and functional groups of BOC are not altered after modification.

The morphology and microstructure of BOC and OV-BOC were surveyed by SEM and TEM (Fig. 2). It is obvious that both BOC and OV-BOC products prepared by the facile solution precipitation method consist of irregular nanoplates with uniform thickness of about 20 nm (Fig. 2A and D). The size of BOC nanoplate was about 50–500 nm which

was a bit larger than that of OV-BOC (50–200 nm). The TEM images of BOC (Fig. 2B) and OV-BOC (Fig. 2E) also confirmed the nanoplate morphology. The lattice fringe of BOC HRTEM image manifested the 0.38 nm interplanar spacing which matched with {010} facet. From the TEM image of OV-BOC (Fig. 2E), one can see that the nanoplates expose two kinds of facets in the top view, namely, basal facet and side facet. HRTEM images of two kinds of facets were exhibited (Fig. 2F and G). Fig. 2F exhibited that the interplanar spacing of the lattice fringe for side facet was 0.68 nm, which is attributed to the {002} facet. Fig. 2G and H shows the HRTEM image of basal facet of the nanoplates. The fast Fourier transition pattern (Fig. 2I) of Fig. 2H revealed that two sets of lattice fringes with interplanar spacing of 0.38 nm and 0.27 nm, respectively, which correspond to the (010) and (110) planes of tetragonal BOC. These evidences all confirmed that {002} facet is the dominant exposing facet of OV-BOC single-crystal nanoplates [31]. Besides, it is worth noticing that the edge of OV-BOC nanosheet was damaged which demonstrate the existence of oxygen vacancy on the surface of OV-BOC.

DRS spectra were recorded to investigate the optical absorption of BOC and OV-BOC (Fig. 3A). The absorption edge of BOC was about 360 nm, indicating that BOC was unable to absorb visible light, which agrees with the previous report [22]. Compared with BOC, OV-BOC exhibits notable visible light absorption between 350 nm and 550 nm, in accordance with the color change from white to pale yellow (inset of Fig. 3A). This photoabsorption feature is a typical manifestation of OV presence [32,33]. To further confirm the existence of OV, EPR was utilized. Fig. 3B shows the EPR spectra of BOC and OV-BOC. There was almost no signal from BOC spectrum. On the contrary, a remarkable signal was observed for OV-BOC at the peak of  $g = 2.001$ , which is a typical signal of OV [12,13,33]. It provides a direct and solid evidence for proving the existence of OV.

The chemical states of related elements and total states density distribution of the valence band of pristine BOC and OV-BOC samples were analyzed by XPS. The survey XPS spectra of both samples revealed that the peaks of three constituent elements Bi 4f, O 1s and C 1s all can be detected (Fig. 3C). The particular peak of C 1s on 284.85 eV was used as the calibration standard. The Bi 4f high resolution XPS spectra (Fig. 3D) exhibited that the two Bi 4f peaks of OV-BOC moved to the direction of low energy by about 0.13 eV, compared with that of BOC. It indicates the appearance of Bi with low chemical valence, and also suggests the presence of OV in the  $[\text{Bi}_2\text{O}_2]^{2+}$  layers of OV-BOC due to charge compensation, because the absence of partial oxygen atoms reduces the coordination number of  $\text{Bi}^{3+}$  leading to the decreased binding energy of Bi 4f [15]. The high resolution spectra of C 1s can be



Scheme 1. Schematic illustration of the preparation for samples (GO here indicates glyoxal).



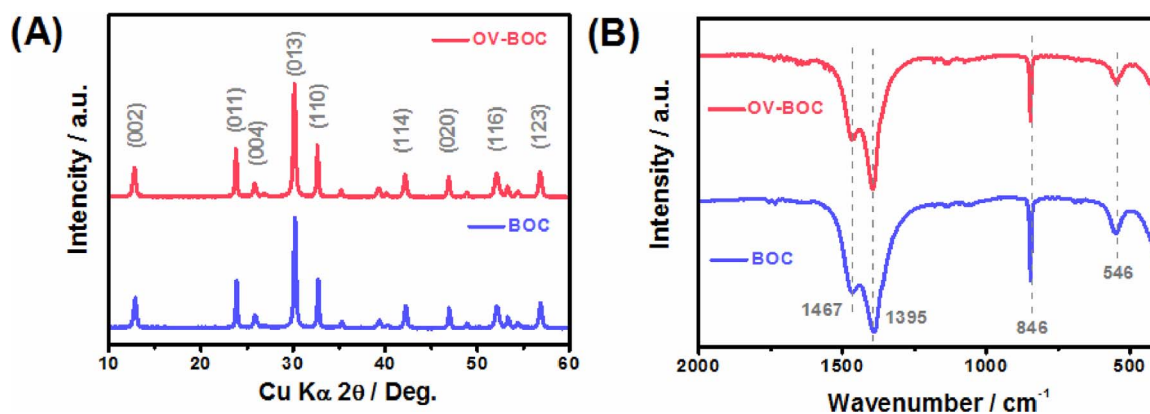


Fig. 1. (A) XRD patterns and (B) FT-IR spectra of pure BOC and OV-BOC photocatalysts.

split into three peaks, which are indexed to the C–O bond in  $[\text{CO}_3]^{2-}$  layers around 289 eV and two particular peaks of the adventitious hydrocarbon of the instrument on 286.22 and 284.85 eV (Fig. 3E) [22]. The C–O binding energy of OV-BOC was lower than that of BOC, which may be also attributed to the lack of oxygen atoms in  $[\text{CO}_3]^{2-}$ . Therefore, the OV may not only exist in the  $[\text{Bi}_2\text{O}_2]^{2+}$  layers, but also reside in the  $[\text{CO}_3]^{2-}$  layers. The O1s spectra (Fig. 3F) can be fitted into three peaks at binding energies of 529.69, 530.62 and 531.28 eV, respectively. The peaks at 529.69 and 530.62 eV were separately the characteristics of C–O bond in  $[\text{Bi}_2\text{O}_2]^{2+}$  layers and Bi–O bond in  $[\text{CO}_3]^{2-}$  layers, and the peak at 531.28 eV was caused by the surface hydroxyl groups adsorbed on photocatalysts [34].

### 3.2. Photocatalytic activity for $\text{H}_2$ evolution, NO removal and antibiotic degradation

The photocatalytic properties of BOC and OV-BOC were

systematically assessed by performing a series of photo-oxidation and reduction reactions, including  $\text{H}_2$  evolution, removal of NO gas and tetracycline hydrochloride (TC) degradation.

The photocatalytic  $\text{H}_2$  evolution of BOC and OV-BOC was evaluated under illumination of a 300 W Xe lamp with 10 vol% MeOH as sacrificial agent and 1 wt% Pt as co-catalyst (Fig. 4A). With 4 h irradiation, the  $\text{H}_2$  production amount over OV-BOC sample reached almost 30  $\mu\text{mol/g}$ . The average  $\text{H}_2$  evolution rate of OV-BOC was 7.1  $\mu\text{mol/g/h}$ , which was nearly 2-fold that of BOC (3.9  $\mu\text{mol/g/h}$ ). NO is a kind of body harmful air pollutant gas that comes from automobile exhaust, so NO removal is meaningful for air purification. As shown in Fig. 4B, BOC gives no activity to remove the NO gas under visible light ( $\lambda > 420 \text{ nm}$ ). In contrast, OV-BOC is efficacious on NO elimination under the visible light, which removes 13% of NO in the continuous flow within 30 min. During the photocatalytic reaction, OV-BOC was exposed to NO and  $\text{O}_2$ . After the lamp was turned on, OV-BOC is capable of absorbing visible light and producing active species which

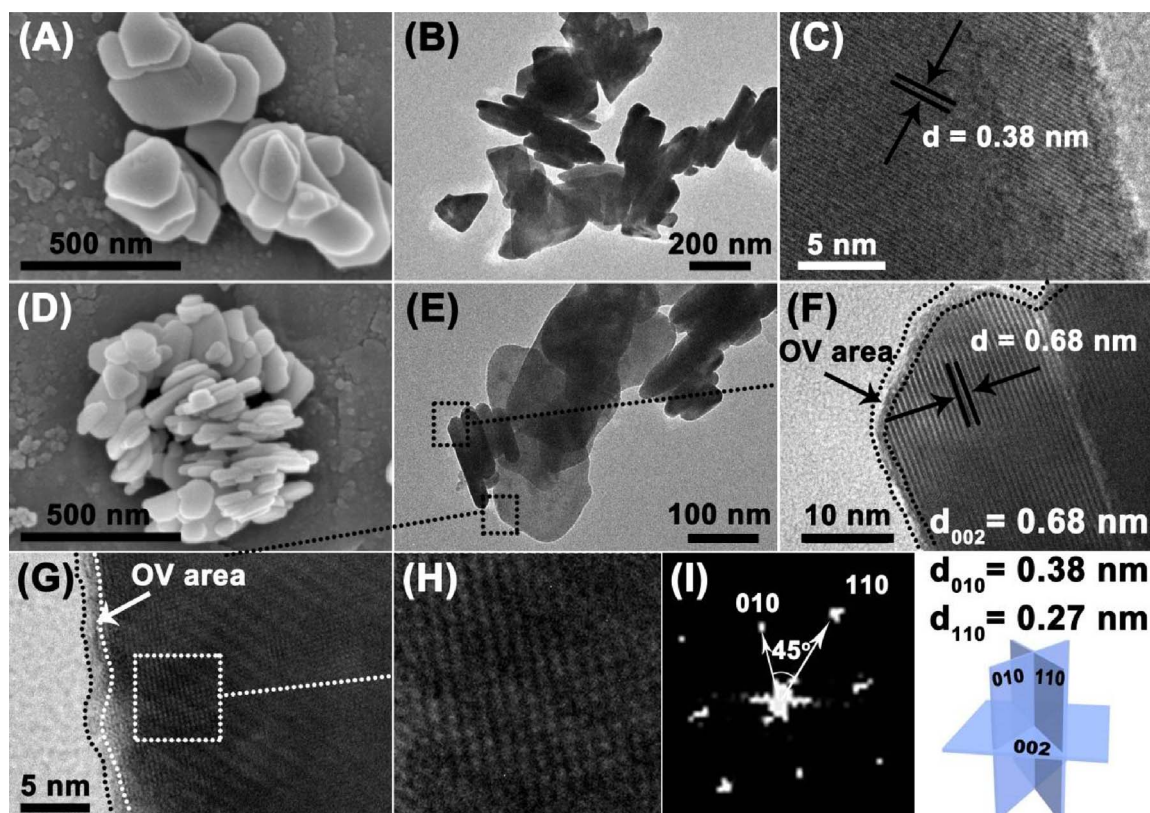


Fig. 2. SEM image (A), TEM image (B) and HRTEM image (C) of BOC; SEM image (D), TEM image (E), HRTEM images (F–H) and HRTEM image FFT (I) of OV-BOC.

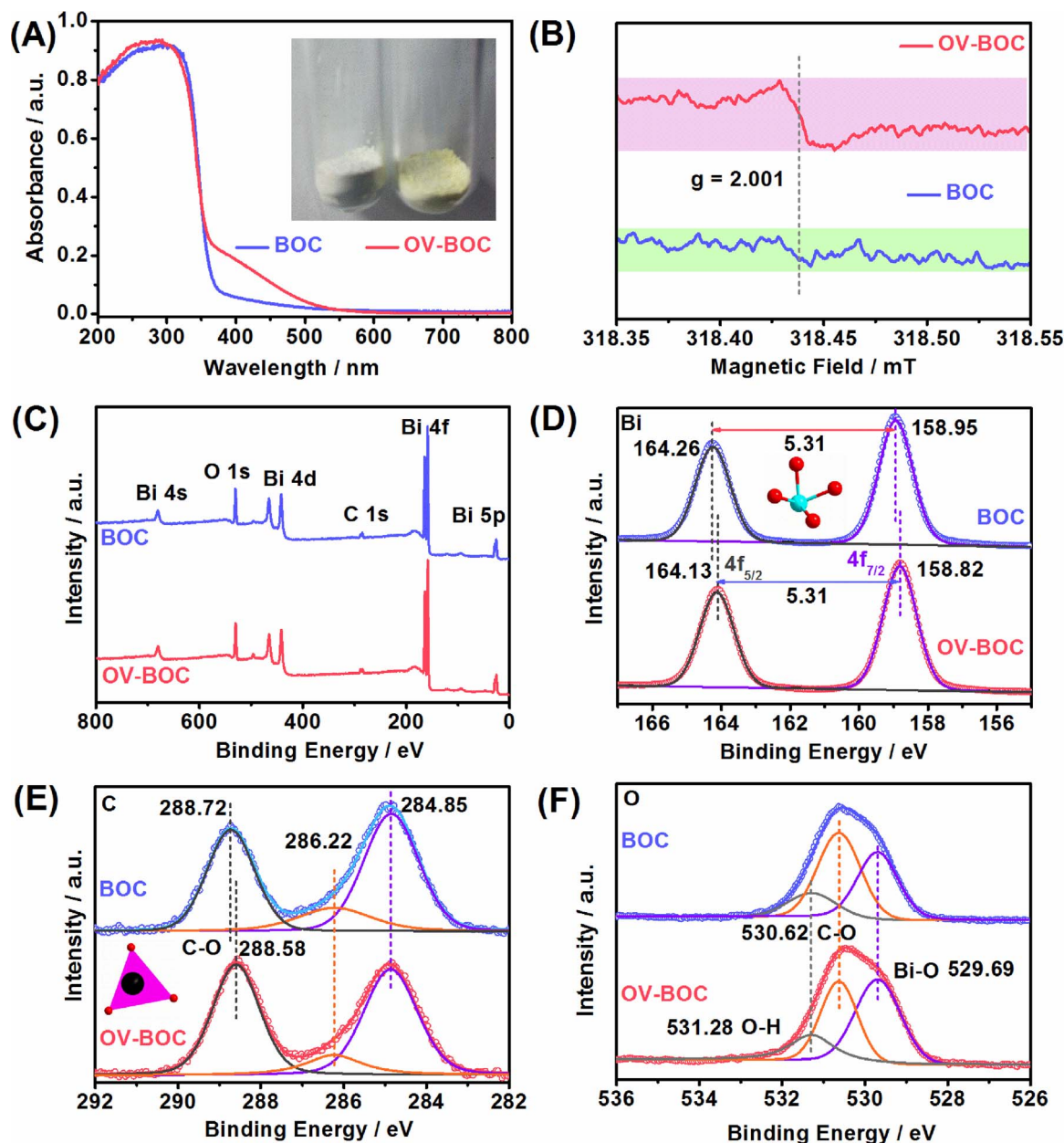
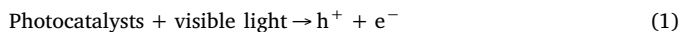


Fig. 3. (A) DRS spectra of BOC and OV-BOC; (B) EPR plots of BOC and OV-BOC; (C) Survey XPS spectra, (D) Bi 4f, (E) C 1s and (F) O 1s of BOC and OV-BOC.

transform NO and O<sub>2</sub> to NO<sub>3</sub><sup>−</sup> and NO<sub>2</sub><sup>−</sup>. The photocatalytic removal of NO may involve following processes [35].



Photocatalysts absorbed the visible light to produce electrons and holes on CB and VB, respectively. Holes reacted with NO and H<sub>2</sub>O to remove NO, and superoxide radicals were generated when electrons reacted with O<sub>2</sub>. Then, superoxide radicals can convert NO to NO<sub>3</sub><sup>−</sup> which is nontoxic.

Tetracycline hydrochloride (TC) as a typical antibiotic remained in waste water can produce large ecological toxicological effects and cause drug resistance of bacterial. The degradation curves of TC over BOC and OV-BOC under visible light ( $\lambda > 420 \text{ nm}$ ) are displayed in Fig. 4C.

After 5 h visible-light irradiation, the concentration of TC was reduced by a half (50%) with OV-BOC, while only 25% of TC was degraded by BOC. This result confirms the highly enhanced visible light photocatalytic activity of OV-BOC. To reveal the active species induced by visible light, the active species trapping experiment was conducted. Potassium iodide (KI), isopropanol (IPA) and nitrogen were introduced as the scavengers to detect holes (h<sup>+</sup>), and hydroxyl radicals ( $\cdot\text{OH}$ ), superoxide radicals ( $\cdot\text{O}_2^-$ ) respectively [36–39]. As displayed in Fig. 4D, the photocatalytic degradation of TC was remarkably inhibited with addition of KI. It demonstrated that holes are the dominant active species and take critical role in the photodegradation process of tetracycline hydrochloride.

The above systematic photocatalytic experiments revealed that the introduction of OV improves not only the photo-reduction capability, but also the photocatalytic oxidation ability of BOC, simultaneously solving the environmental and energy issues. Stability of catalyst is an important factor for practical applications. The H<sub>2</sub> evolution cycle experiment was carried out to inspect the stability and durability of OV-

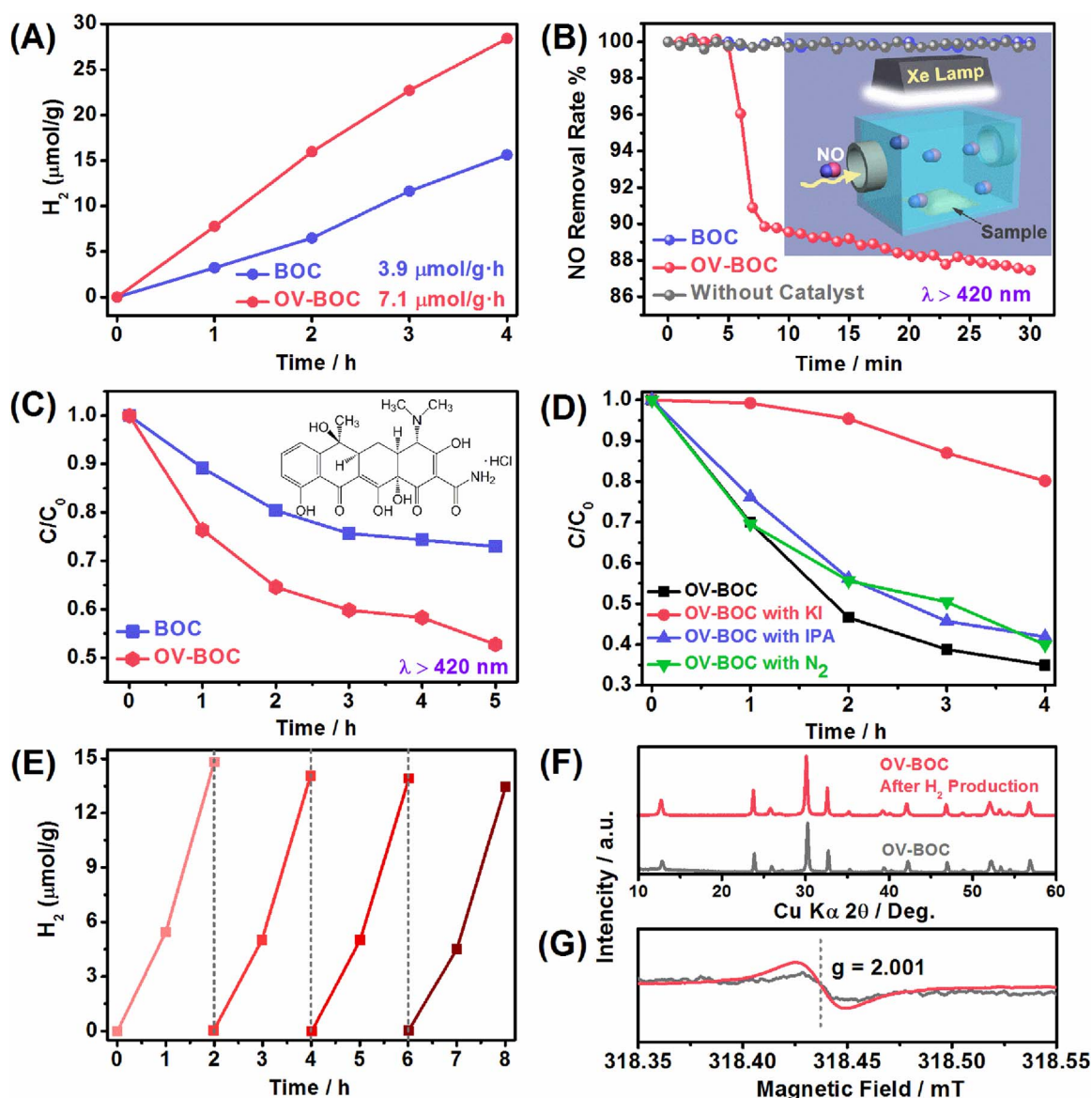


Fig. 4. (A) Photocatalytic  $H_2$  evolution curves over BOC and OV-BOC under simulated solar light irradiation; (B) Photocatalytic removal curves of NO gas over BOC and OV-BOC under the irradiation of visible light ( $\lambda > 420\text{ nm}$ ); (C) Photocatalytic degradation curves of tetracycline hydrochloride over BOC and OV-BOC under visible light ( $\lambda > 420\text{ nm}$ ); (D) Degradation curves of tetracycline hydrochloride with different scavengers over OV-BOC under the visible-light ( $\lambda > 420\text{ nm}$ ); (E) Cyclic runs for the photocatalytic  $H_2$  production; XRD patterns (F) and EPR plots (G) of OV-BOC before and after  $H_2$  evolution reaction.

BOC. After 4 cycles running, the photocatalytic  $H_2$  evolution rate was decreased slightly. Comparing the XRD patterns of OV-BOC before photocatalytic reaction and after  $H_2$  evolution test, one can see that not any changes were observed (Fig. 4F). The EPR spectra of the OV-BOC before and after  $H_2$  generation reaction were also recorded. As illustrated in the new Fig. 4G, the EPR signal of OV-BOC after reaction still maintains well in comparison with that before reaction, which further confirms the stability of OV-BOC.

### 3.3. Band structure evolution

In order to determine the effect of OV on the band structure evolution of BOC, DRS, Mott-Schottky measurement and valence band (VB) XPS (VB-XPS) were performed. Through the transformation based on the Formula (5), the optical absorption curves in Fig. 3A were used to analyze the band gap of BOC and OV-BOC. Optical absorption and band gap of semiconductors adhere to the following Kubelka–Munk (KM) formula [40], where the band gap can be determined

$$ah\nu = A(h\nu - E_g)^{n/2} \quad (5)$$

Where  $h$ ,  $\nu$ ,  $A$ ,  $\alpha$ , and  $E_g$  are the Planck constant, photon frequency, a constant, optical absorption coefficient, and band gap, respectively. The value of variable number  $n$  depended on the types of electronic transitions:  $n = 1$  or  $4$  for direct-allowed or indirect-allowed transition, respectively. BOC is an indirect-allowed semiconductor, so that the value of  $n$  is  $4$  [22]. The band gap values of BOC and OV-BOC were shown in Fig. 5A. The band gap value of BOC was  $3.37\text{ eV}$  which was consistent with the previous report [21–23]. Two band gaps for OV-BOC are found, which are  $3.37\text{ eV}$  and  $2.25\text{ eV}$ , respectively. It is in accordance with the fact that oxygen vacancy always causes tail absorption. Mott-Schottky curves can reflect the flat band (FB) potential and semiconductor type of semiconductor material. As shown in Fig. 5B, the positive slope demonstrates that both BOC and OV-BOC are  $n$ -type semiconductors [22]. For  $n$ -type semiconductor, the FB potential is close to the conduction band (CB), and thus the difference in FB potential can indicate the CB difference. As the FB potentials of BOC and OV-BOC are determined to be same, the CB of OV-BOC is similar to



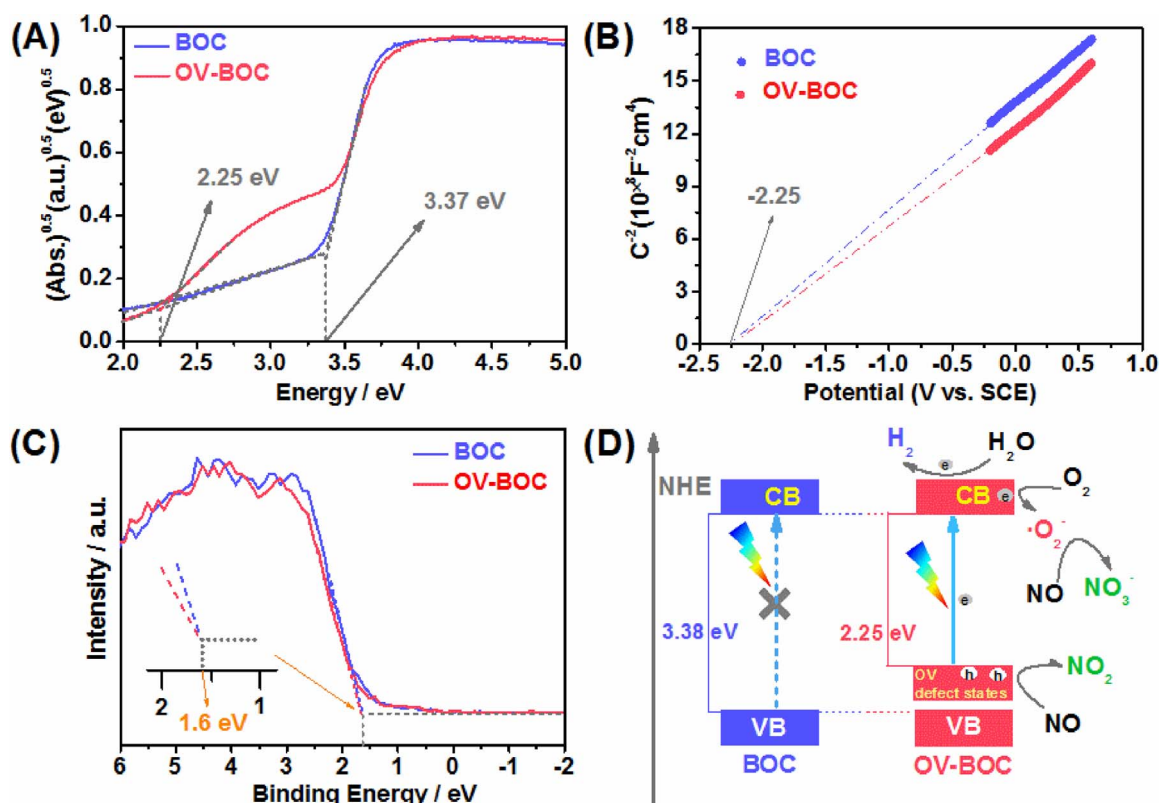


Fig. 5. (A) Band gaps, (B) Mott-Schottky plots, (C) VB-XPS spectra and (D) Schematic band structure of BOC and OV-BOC.

BOC. Besides, the VB-XPS also indicates that the VB positions of them are the same (Fig. 5C). Summing up the above results, we can describe the band structure of BOC and OV-BOC using a schematic diagram (Fig. 5D). OV introduces defect states between CB and VB, favoring the transition of electrons in the forbidden band [32]. Therefore, compared to BOC, OV-BOC is endowed with intensive visible light absorption and narrowed band gap. Under visible light ( $\lambda > 420$  nm), BOC is almost not activated, while for OV-BOC, the electron-hole pairs can be activated and separated. The photogenerated electrons of OV-BOC would transfer onto CB, and the photoinduced holes remain at the OV defect states. Then, the photon-generated carriers react with the contaminants, such as NO and TC, during the photodegradation process. With respect to  $\text{H}_2$  evolution under simulated solar light irradiation, more photoinduced electrons are generated due to the much enhanced photoabsorption of OV-BOC, thus resulting in higher photocatalytic  $\text{H}_2$  production activity. In addition, charge separation as another factor that significantly influences the photo-reactivity is also taken into account, which is investigated and discussed in the following.

### 3.4. Charge separation and photocatalytic activity enhancement mechanism

The photocatalytic activity of a semiconductor material is intimately associated with the charge carrier density, bulk charge separation, movement on the surface of material and interfacial transfer of photogenerated charges. In order to systematically survey the movement action for photogenerated charges, photoelectrochemical and photoelectric measurements were carried out, including transient photocurrent response, I–V measurement, EIS and SPV. The transient photocurrent response curves under visible light ( $\lambda > 420$  nm) are shown in Fig. 6A, and the photocurrent density of OV-BOC was 2.5 times as high as that of BOC. It demonstrated that much more photo-excited electrons are produced for OV-BOC with illumination of visible light. Another useful information was obtained by measuring the photocurrent responses of BOC and OV-BOC under different wavelengths of

visible light (420, 450, 500, 550, and 600 nm). It is seen that OV-BOC shows higher current density than BOC at almost all the wavelengths, but the enhancement degree gradually decreases with increasing the illumination wavelength. This observation is in accordance with the fact that the photoabsorption of BOC and OV-BOC tends to be consistent at longer wavelength (Fig. 6B). The continuous photocurrent response between 400 and 600 nm confirms the above conclusion (Fig. 6C), and also uncovers that the degradation or  $\text{H}_2$  production activities originate from photocatalysis.

The density of charge carriers is a significant parameter to evaluate the photocatalyst material. Large carrier density usually contributes to higher photocatalytic performance of photocatalyst. In the quasi Fermi level, the carrier density difference can be calculated by the Nernst equation [41],

$$E_{f1} - E_{f2} = kT \ln(N_{f1}/N_{f2})/e \quad (6)$$

herein,  $E_{f1}$ ,  $E_{f2}$  ( $x = f1, f2$ ),  $k$ ,  $T$  and  $e$  are the quasi Fermi level, carrier density, the Boltzmann constant, temperature and elementary charge. When methylviologen dichloride ( $\text{MVCl}_2$ ) serves as the fast electron acceptor, the photocurrent onset potential in a voltammogram test can be regarded as the quasi Fermi level of majority carriers. In the I–V plot (Fig. 6D), the photocurrent onset potentials of BOC and OV-BOC are  $-0.21$  and  $-0.25$  V, respectively. Based on the above Nernst equation, the carrier density of OV-BOC is determined as 4.7 times larger than that of BOC. EIS can detect the charge transfer efficiency on the surface of photocatalyst. A smaller arc radius indicates a higher charge transfer efficiency [20,42,43]. As seen from Fig. 6E, OV-BOC shows an evidently smaller arc radius than BOC, evidencing the emigration and transfer efficiencies of charge carriers were improved because of the existence of OV. Finally, the photogenerated carrier separation efficiency in bulk phase was demonstrated by the SPV spectra. It is obvious that OV-BOC displays a remarkably higher photovoltage barrier than BOC in the range of visible light region, meaning promoted bulk charge separation (Fig. 6F). The above series results unearth that the charge carrier

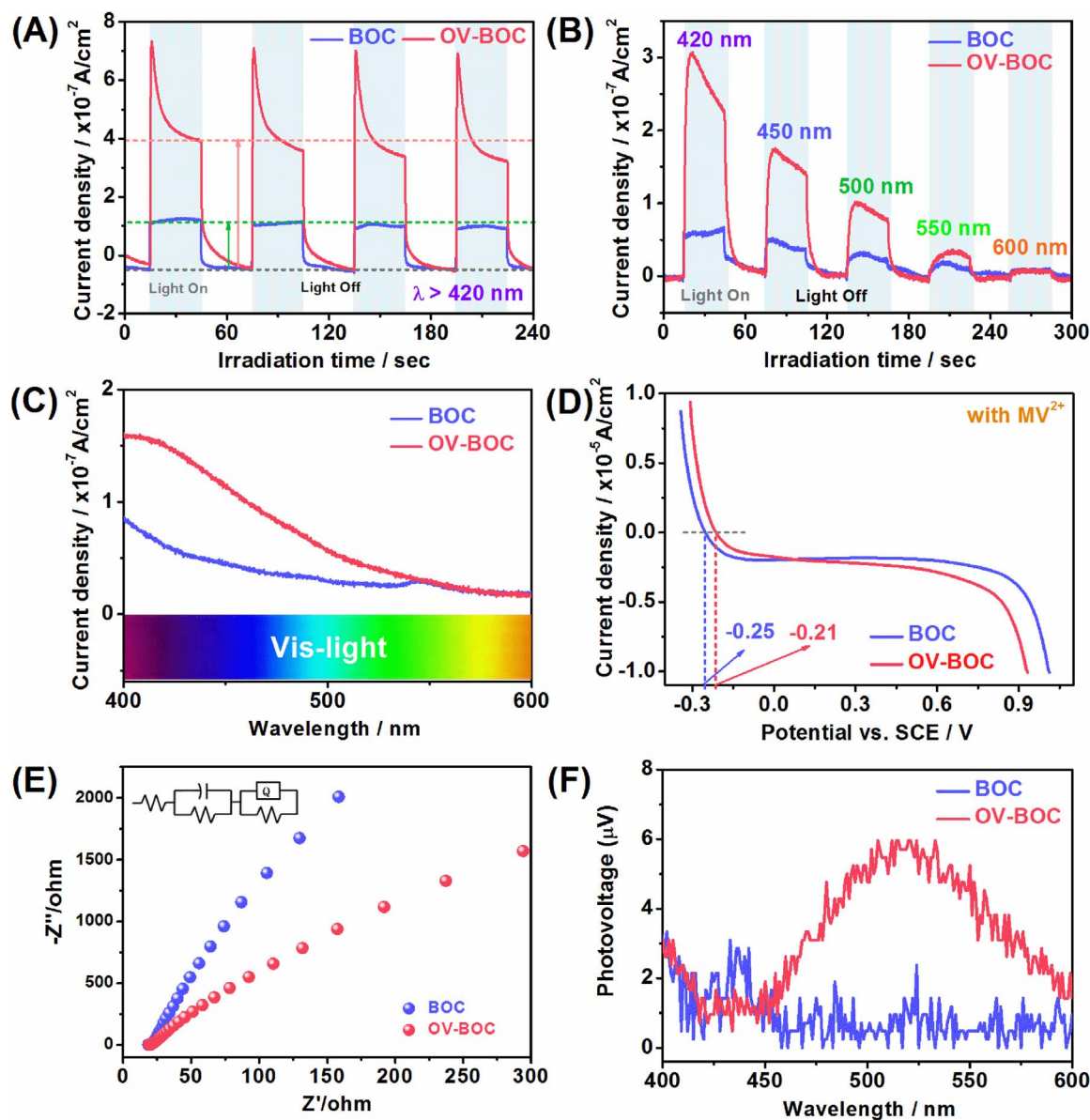


**Fig. 6.** (A) Transient photocurrent response of BOC and OV-BOC under visible light ( $\lambda > 420$  nm) illumination; (B) Photocurrent response of BOC and OV-BOC under different wavelengths of visible light; (C) Photocurrent response under continuous visible light (400–600 nm); (D) I–V curves of BOC and OV-BOC; (E) EIS plots of BOC and OV-BOC; (F) SPV spectra of BOC and OV-BOC.

density, bulk charge separation, surface and interfacial transfer of photogenerated charges are all greatly facilitated.

### 3.5. Facile formation of concentration-adjustable oxygen vacancy

In view of that the generation of OV in BOC was caused by the reducibility of glyoxal, different volumes of glyoxal added were taken into account to control the OV concentration. To prove the advantage of the current method, a series of OV-BOC samples with different OV concentrations (OV-BOC #1, OV-BOC #2 and OV-BOC #3) were prepared by addition of glyoxal with different volumes (2 mL, 3 mL and 4 mL) into Bi(NO<sub>3</sub>)<sub>3</sub>·5H<sub>2</sub>O solution. From the DRS spectra of those samples (Fig. 7A), it is evident to note that the visible light absorption of OV-BOC gradually enhances with raising the volume of glyoxal in the reactant solution, consistent with the color change from white to pale brown (Fig. 7B). To verify that the photoabsorption variation is resulted by OV concentration change, the EPR spectra of OV-BOC #1, OV-BOC #2 and OV-BOC #3 are displayed (Fig. 7C). Remarkably, the OV signal at  $g = 2.001$  orderly strengthens from OV-BOC #1 to OV-BOC #3,

which is in positive correlation with the volume of glyoxal. On the basis of the above observations, we can safely conclude that the concentration of OV can be precisely controlled by the volume of glyoxal. This would allow the well optimization and balance between the light absorption and the band energy levels (oxidation/reduction driving force). The photocatalytic performance of H<sub>2</sub> evolution under simulated solar light irradiation, NO gas removal, tetracycline hydrochloride degradation under visible light ( $\lambda > 420$  nm) over BOC and OV-BOC #1, 2, 3 are also carried out. The H<sub>2</sub> evolution graph (Fig. 7D) displays that the photocatalytic activity of OV-BOC #1 and 2 is higher than that of BOC and OV-BOC #1 is the optimum sample. But the H<sub>2</sub> evolution performance of OV-BOC #3 is even lower than the performance of BOC. Photocatalytic removal curves of NO gas indicate that all the modified samples with oxygen vacancy show visible-light photocatalytic activity. In contrast, BOC cannot remove NO gas under visible light. After 30 min photoreaction process, OV-BOC #1 exhibits the best photocatalytic activity. The photocatalytic degradation curves exhibit a similar trend with H<sub>2</sub> evolution ones that OV-BOC #1 shows the best activity and performance of OV-BOC #3 is inferior to BOC. Thus, it can be



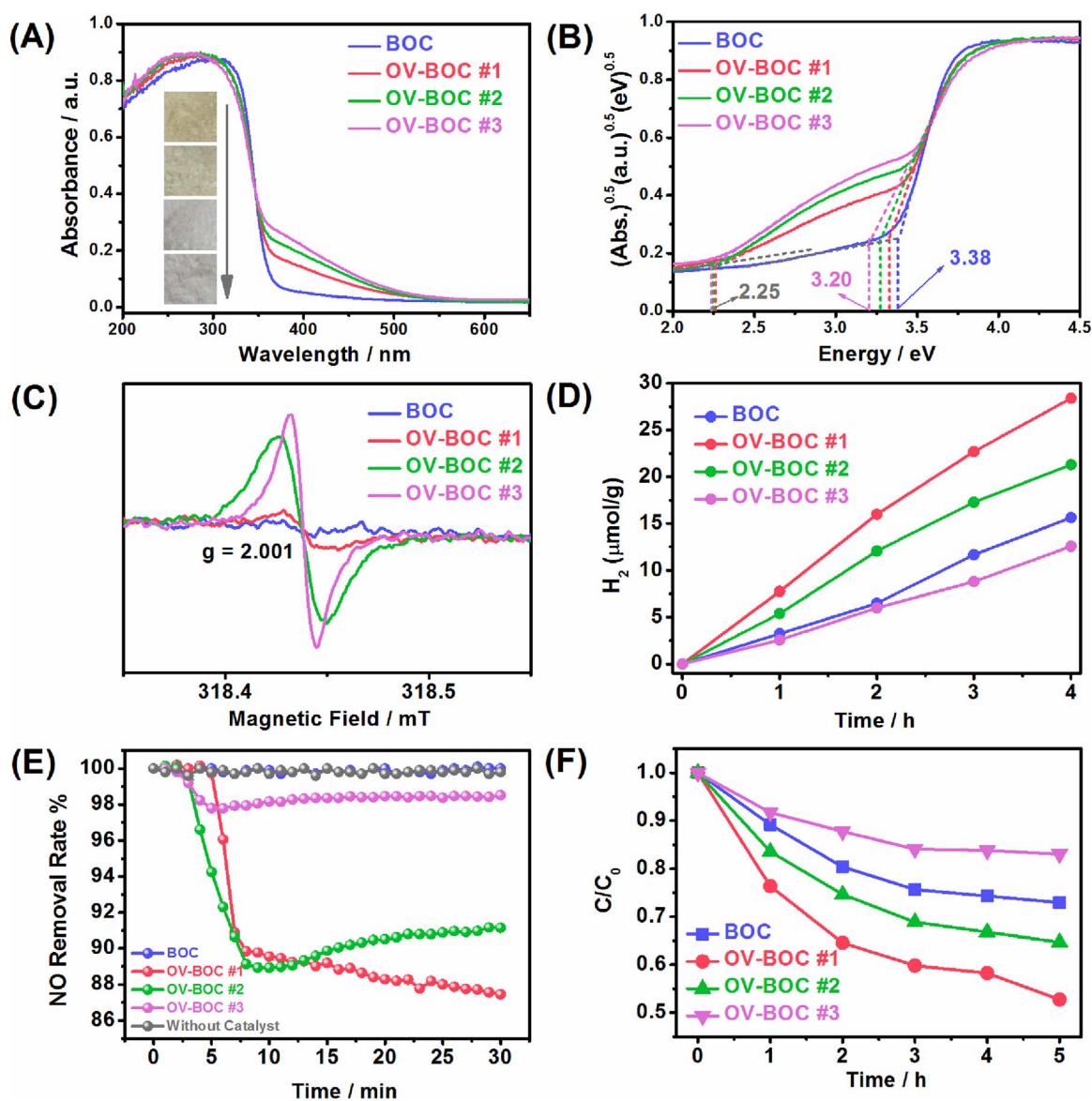


Fig. 7. DRS spectra (A), band gap (B) and EPR plots (C) of BOC and OV-BOC #1, 2, 3; (D) photocatalytic  $\text{H}_2$  evolution curves over BOC and OV-BOC #1, 2, 3 under simulated solar light irradiation; photocatalytic removal curves of NO gas (E) and photocatalytic degradation curves of tetracycline hydrochloride (F) over BOC and OV-BOC #1, 2, 3 under visible light ( $\lambda > 420 \text{ nm}$ ).

concluded that excessive defects in OV-BOC #3 lead to poor photocatalytic performance, which may be from the destroyed crystal structure and serious recombination of photogenerated electrons and holes. Based on these analyses, introduction of oxygen vacancies with appropriate level is critical to the photocatalytic activity. Therefore, it is expected to achieve smart design of high-performance photocatalysts for the solar energy conversion applications by oxygen vacancy engineering.

#### 4. Conclusions

In summary, oxygen vacancy (OV) concentration tunable  $\text{Bi}_2\text{O}_2\text{CO}_3$  photocatalyst was synthesized by a facile and low-cost glyoxal-assisted solution precipitation route at room temperature, and the OV occurs in both  $[\text{Bi}_2\text{O}_2]^{2+}$  layers and  $[\text{CO}_3]^{2-}$  layers of BOC. Due to the existence of OV, the defect energy level is also introduced, which results in greatly enhanced photoabsorption of OV-BOC. Systematic photoelectrochemical and photoelectric measurements demonstrated that the carriers density in OV-BOC increases by 4.7-fold, and the bulk and surface carrier separation and interfacial carrier charge migration are

all profoundly promoted. Profiting from these virtues, compared with BOC, OV-BOC presents highly enhanced photocatalytic activity for degradation of NO and tetracycline hydrochloride under visible light ( $\lambda > 420 \text{ nm}$ ) as well as improved photocatalytic  $\text{H}_2$  production performance. Moreover, the adjustable OV concentration of BOC is easily realized by simply controlling the addition content of glyoxal, which is beneficial to optimizing the photoabsorption and redox-ability. The study offers new insight into fabrication of oxygen vacancy-mediated high-performance photocatalytic materials for solar energy utilization.

#### Acknowledgements

This work was jointly supported by the National Natural Science Foundations of China (No. 51672258 and 51572246), the Fundamental Research Funds for the Central Universities (2652015296).

#### References

- [1] H. Wang, L. Zhang, Z. Chen, J. Hu, S. Li, Z. Wang, J. Liu, X. Wang, Semiconductor heterojunction photocatalysts: design, construction, and photocatalytic

- performances, *Chem. Soc. Rev.* 43 (2014) 5234–5244.
- [2] Y. Ma, X. Wang, Y. Jia, X. Chen, H. Han, C. Li, Titanium dioxide-based nanomaterials for photocatalytic fuel generations, *Chem. Rev.* 114 (2014) 9987–10043.
  - [3] Z. Bian, F. Cao, J. Zhu, H. Li, Plant uptake-assisted round-the-clock photocatalysis for complete purification of aquaculture wastewater using sunlight, *Environ. Sci. Technol.* 49 (2015) 2418–2424.
  - [4] Y.L. Li, Y.Y. Bian, H.X. Qin, Y.X. Zhang, Z.F. Bian, Photocatalytic reduction behavior of hexavalent chromium on hydroxyl modified titanium dioxide, *Appl. Catal. B* 206 (2017) 293–299.
  - [5] T. Shi, W. Chang, H. Zhang, H. Ji, W. Ma, C. Chen, J. Zhao, H<sub>2</sub>O-involved two-electron pathway for photooxidation of aldehydes on TiO<sub>2</sub>: an isotope labeling study, *Environ. Sci. Technol.* 49 (2015) 3024–3031.
  - [6] M.K. Nowotny, L.R. Sheppard, T. Bak, J. Nowotny, Defect chemistry of titanium dioxide. Application of defect engineering in processing of TiO<sub>2</sub>-based photocatalysts†, *J. Phys. Chem. C* 112 (2008) 5275–5300.
  - [7] X. Chen, L. Liu, P.Y. Yu, S.S. Mao, Increasing solar absorption for photocatalysis with black hydrogenated titanium dioxide nanocrystals, *Science* 331 (2011) 746–750.
  - [8] H. Li, J. Li, Z. Ai, F. Jia, L. Zhang, Oxygen vacancy-mediated photocatalysis of BiOCl: reactivity, selectivity, and perspectives, *Angew. Chem. Int. Ed. Engl.* 57 (2018) 122–138.
  - [9] N. Zhang, X. Li, H. Ye, S. Chen, H. Ju, D. Liu, Y. Lin, W. Ye, C. Wang, Q. Xu, J. Zhu, L. Song, J. Jiang, Y. Xiong, Oxide defect engineering enables to couple solar energy into oxygen activation, *J. Am. Chem. Soc.* 138 (2016) 8928–8935.
  - [10] X.J. Wang, Y. Zhao, F.T. Li, L.J. Dou, Y.P. Li, J. Zhao, Y.J. Hao, A chelation strategy for in-situ constructing surface oxygen vacancy on {001} facets exposed BiOBr nanosheets, *Sci. Rep.* 6 (2016) 24918.
  - [11] F. Dong, T. Xiong, Y. Sun, H. Huang, Z. Wu, Synergistic integration of thermocatalysis and photocatalysis on black defective (BiO)<sub>2</sub>CO<sub>3</sub> microspheres, *J. Mater. Chem. A* 3 (2015) 18466–18474.
  - [12] Y. Lv, Y. Liu, Y. Zhu, Y. Zhu, Surface oxygen vacancy induced photocatalytic performance enhancement of a BiPO<sub>4</sub> nanorod, *J. Mater. Chem. A* 2 (2014) 1174–1182.
  - [13] Y. Lv, W. Yao, R. Zong, Y. Zhu, Fabrication of wide-range-visible photocatalyst Bi<sub>2</sub>WO<sub>6-x</sub> nanoplates via surface oxygen vacancies, *Sci. Rep.* 6 (2016) 19347.
  - [14] H. Li, J. Shang, Z. Ai, L. Zhang, Efficient visible light nitrogen fixation with BiOBr nanosheets of oxygen vacancies on the exposed {001} facets, *J. Am. Chem. Soc.* 137 (2015) 6393–6399.
  - [15] Z. Zhao, Y. Zhou, F. Wang, K. Zhang, S. Yu, K. Cao, Polyaniline-decorated {001} facets of Bi<sub>2</sub>O<sub>2</sub>CO<sub>3</sub> nanosheets: in situ oxygen vacancy formation and enhanced visible light photocatalytic activity, *ACS Appl. Mater. Interfaces* 7 (2015) 730–737.
  - [16] H. Fu, C. Pan, W. Yao, Y. Zhu, Visible-light-induced degradation of rhodamine B by nanosized Bi<sub>2</sub>WO<sub>6</sub>, *J. Phys. Chem. B* 109 (2005) 22432–22439.
  - [17] L.W. Zhang, T.G. Xu, X. Zhao, Y.F. Zhu, Controllable synthesis of Bi<sub>2</sub>MoO<sub>6</sub> and effect of morphology and variation in local structure on photocatalytic activities, *Appl. Catal. B* 98 (2010) 138–146.
  - [18] X. Zhang, Z. Ai, F. Jia, L. Zhang, Generalized one-pot synthesis characterization, and photocatalytic activity of hierarchical BiOX (X = Cl, Br, I) nanoplate microspheres, *J. Phys. Chem. C* 112 (2008) 747–753.
  - [19] J. Jiang, K. Zhao, X. Xiao, L. Zhang, Synthesis and facet-dependent photoreactivity of BiOCl single-crystalline nanosheets, *J. Am. Chem. Soc.* 134 (2012) 4473–4476.
  - [20] Y. Sun, H. Cheng, S. Gao, Z. Sun, Q. Liu, Q. Liu, F. Lei, T. Yao, J. He, S. Wei, Y. Xie, Freestanding tin disulfide single-layers realizing efficient visible-light water splitting, *Angew. Chem. Int. Ed. Engl.* 51 (2012) 8727–8731.
  - [21] Y. Zheng, F. Duan, M.Q. Chen, Y. Xie, Synthetic Bi<sub>2</sub>O<sub>2</sub>CO<sub>3</sub> nanostructures: novel photocatalyst with controlled special surface exposed, *J. Mol. Catal. A: Chem.* 317 (2010) 34–40.
  - [22] H.W. Huang, X.W. Li, J.J. Wang, F. Dong, P.K. Chu, T.R. Zhang, Y.H. Zhang, Anionic group self-doping as a promising strategy: band-gap engineering and multi-functional applications of high-performance CO<sub>3</sub><sup>2-</sup>-doped Bi<sub>2</sub>O<sub>2</sub>CO<sub>3</sub>, *ACS Catal.* 5 (2015) 4094–4103.
  - [23] Q. Li, H. Liu, F. Dong, M. Fu, Hydrothermal formation of N-doped (BiO)<sub>2</sub>CO<sub>3</sub> honeycomb-like microspheres photocatalysts with bismuth citrate and dicyandiamide as precursors, *J. Colloid Interface Sci.* 408 (2013) 33–42.
  - [24] H.W. Huang, J.J. Wang, F. Dong, Y.X. Guo, N. Tian, Y.H. Zhang, T.R. Zhang, Highly efficient Bi<sub>2</sub>O<sub>2</sub>CO<sub>3</sub> single-crystal lamellae with dominantly exposed {001} facets, *Cryst. Growth Des.* 15 (2015) 534–537.
  - [25] X.C. Zhang, T.Y. Guo, X.W. Wang, Y.W. Wang, C.M. Fan, H. Zhang, Facile composition-controlled preparation and photocatalytic application of BiOCl/Bi<sub>2</sub>O<sub>2</sub>CO<sub>3</sub> nanosheets, *Appl. Catal. B* 150 (2014) 486–495.
  - [26] L.L. Zhang, C. Hu, H.H. Ji, p-AgI anchored on {001} facets of n-Bi<sub>2</sub>O<sub>2</sub>CO<sub>3</sub> sheets with enhanced photocatalytic activity and stability, *Appl. Catal. B* 205 (2017) 34–41.
  - [27] P. Madhusudan, J.R. Ran, J. Zhang, J.G. Yu, G. Liu, Novel urea assisted hydrothermal synthesis of hierarchical BiVO<sub>4</sub>/Bi<sub>2</sub>O<sub>2</sub>CO<sub>3</sub> nanocomposites with enhanced visible-light photocatalytic activity, *Appl. Catal. B* 110 (2011) 286–295.
  - [28] M.C. Long, P.D. Hu, H.D. Wu, J. Cai, B.H. Tan, B.X. Zhou, Efficient visible light photocatalytic heterostructure of nonstoichiometric bismuth oxyiodide and iodine intercalated Bi<sub>2</sub>O<sub>2</sub>CO<sub>3</sub>, *Appl. Catal. B* 184 (2016) 20–27.
  - [29] R. Flamini, A. Dalla Vedova, Glyoxal/glycolaldehyde: a redox system involved in malolactic fermentation of wine, *J. Agric. Food Chem.* 51 (2003) 2300–2303.
  - [30] H. Huang, K. Xiao, S. Yu, F. Dong, T. Zhang, Y. Zhang, Iodide surface decoration: a facile and efficacious approach to modulating the band energy level of semiconductors for high-performance visible-light photocatalysis, *Chem. Commun.* 52 (2016) 354–357.
  - [31] F. Dong, Q. Li, W. Zhang, M. Guan, W.-K. Ho, Z. Wu, Synthesis of flower-like, pinon-like and faceted nanoplates (BiO)<sub>2</sub>CO<sub>3</sub> micro/nanostructures with morphology-dependent photocatalytic activity, *Mater. Chem. Phys.* 142 (2013) 381–386.
  - [32] Y. Lv, Y. Zhu, Y. Zhu, Enhanced photocatalytic performance for the BiPO<sub>4-x</sub> nanorod induced by surface oxygen vacancy, *J. Phys. Chem. C* 117 (2013) 18520–18528.
  - [33] L. Ye, K. Deng, F. Xu, L. Tian, T. Peng, L. Zan, Increasing visible-light absorption for photocatalysis with black BiOCl, *Phys. Chem. Chem. Phys.* 14 (2012) 82–85.
  - [34] J. Fu, B. Zhu, C. Jiang, B. Cheng, W. You, J. Yu, Hierarchical porous O-doped g-C<sub>3</sub>N<sub>4</sub> with enhanced photocatalytic CO<sub>2</sub> reduction activity, *Small* 13 (2017).
  - [35] J. Luo, G. Dong, Y. Zhu, Z. Yang, C. Wang, Switching of semiconducting behavior from n-type to p-type induced high photocatalytic NO removal activity in g-C<sub>3</sub>N<sub>4</sub>, *Appl. Catal. B* 214 (2017) 46–56.
  - [36] O.I. Micic, Y. Zhang, K.R. Cromack, A.D. Trifunac, M.C. Thurnauer, Trapped holes on titania colloids studied by electron paramagnetic resonance, *J. Phys. Chem.* 97 (1993) 7277–7283.
  - [37] H.W. Huang, K. Xiao, Y. He, T.R. Zhang, F. Dong, X. Du, Y.H. Zhang, In situ assembly of BiOI@Bi<sub>12</sub>O<sub>17</sub>Cl<sub>2</sub> p-n junction: charge induced unique front-lateral surfaces coupling heterostructure with high exposure of BiOI {001} active facets for robust and nonselective photocatalysis, *Appl. Catal. B* 199 (2016) 75–86.
  - [38] H. Huang, X. Han, X. Li, S. Wang, P.K. Chu, Y. Zhang, Fabrication of multiple heterojunctions with tunable visible-light-active photocatalytic reactivity in BiOBr-BiOI full-range composites based on microstructure modulation and band structures, *ACS Appl. Mater. Interfaces* 7 (2015) 482–492.
  - [39] C. Tang, L. Liu, Y. Li, Z. Bian, Aerosol spray assisted assembly of TiO<sub>2</sub> mesocrystals into hierarchical hollow microspheres with enhanced photocatalytic performance, *Appl. Catal. B* 201 (2017) 41–47.
  - [40] Y. Ohko, K. Hashimoto, A. Fujishima, Kinetics of photocatalytic reactions under extremely low-intensity UV illumination on titanium dioxide thin films, *J. Phys. Chem. A* 101 (1997) 8057–8062.
  - [41] Z. Hu, L. Yuan, Z. Liu, Z. Shen, J.C. Yu, An elemental phosphorus photocatalyst with a record high hydrogen evolution efficiency, *Angew. Chem. Int. Ed. Engl.* 55 (2016) 9580–9585.
  - [42] F. Chen, F. Cao, H. Li, Z. Bian, Exploring the important role of nanocrystals orientation in TiO<sub>2</sub> superstructure on photocatalytic performances, *Langmuir* 31 (2015) 3494–3499.
  - [43] H.W. Huang, K. Xiao, X. Du, Y.H. Zhang, Vertically aligned nanosheets-array-like BiOI homojunction: three-in-one promoting photocatalytic oxidation and reduction abilities, *ACS Sustain. Chem. Eng.* 5 (2017) 5253–5264.